Zigzag antiferromagnetic quantum ground state in monoclinic honeycomb lattice antimonates $A_3Ni_2SbO_6$ (A = Li, Na)

E. A. Zvereva,[1,*] M. I. Stratan,[1] Y. A. Ovchenkov,[1] V. B. Nalbandyan,[2] J.-Y. Lin,[3] E. L. Vavilova,[4] M. F. Iakovleva,[4] M. Abdel-Hafiez,[5,6,7] A. V. Silhanek,[5] X.-J. Chen,[7] A. Stroppa,[8] S. Picozzi,[8] H. O. Jeschke,[9] R. Valentí,[9] and A. N. Vasiliev[1,10,11]

[1]*Faculty of Physics, Moscow State University, 119991 Moscow, Russia*
[2]*Chemistry Faculty, Southern Federal University, 344090 Rostov-on-Don, Russia*
[3]*National Chiao Tung University, Hsinchu, Taiwan, 300 Republic of China*
[4]*Zavoisky Physical-Technical Institute (ZPhTI) of the Kazan Scientific Center of the Russian Academy of Sciences, 420029 Kazan, Russia*
[5]*Département de Physique, Liége University-Belgium, B-4000 Liege, Belgium*
[6]*Faculty of Science, Physics Department, Fayoum University, 63514 Fayoum, Egypt*
[7]*Center for High Pressure Science and Technology Advanced Research, 1690 Cailun Road, Shanghai, 201203, China*
[8]*Consiglio Nazionale delle Ricerche (CNR) SPIN, 67010 Coppito, L'Aquila, Italy*
[9]*Institut für Theoretische Physik, Goethe-Universität Frankfurt, Max-von-Laue-Straße 1, 60438 Frankfurt am Main, Germany*
[10]*Theoretical Physics and Applied Mathematics Department, Ural Federal University, 620002 Ekaterinburg, Russia*
[11]*National University of Science and Technology "MISiS," Moscow 119049, Russia*

(Received 26 May 2015; revised manuscript received 28 August 2015; published 1 October 2015)

We present a comprehensive experimental and theoretical study of the electronic and magnetic properties of two quasi-two-dimensional (2D) honeycomb lattice monoclinic compounds $A_3Ni_2SbO_6$ (A = Li, Na). Magnetic susceptibility and specific heat data are consistent with the onset of antiferromagnetic long-range order with Néel temperatures of ~14 and 16 K for $Li_3Ni_2SbO_6$ and $Na_3Ni_2SbO_6$, respectively. The effective magnetic moments of 4.3 μ_B/f.u. ($Li_3Ni_2SbO_6$) and 4.4 μ_B/f.u. ($Na_3Ni_2SbO_6$), where f.u. is formula units, indicate that Ni^{2+} is in a high-spin configuration ($S = 1$). The temperature dependence of the inverse magnetic susceptibility follows the Curie-Weiss law in the high-temperature region and shows positive values of the Weiss temperature, ~8 K ($Li_3Ni_2SbO_6$) and ~12 K ($Na_3Ni_2SbO_6$), pointing to the presence of nonnegligible ferromagnetic interactions, although the system orders antiferromagnetically at low temperatures. In addition, the magnetization curves reveal a field-induced (spin-flop type) transition below T_N that can be related to the magnetocrystalline anisotropy in these systems. These observations are in agreement with density functional theory calculations, which show that both antiferromagnetic and ferromagnetic intralayer spin exchange couplings between Ni^{2+} ions are present in the honeycomb planes, supporting a zigzag antiferromagnetic ground state. Based on our experimental measurements and theoretical calculations, we propose magnetic phase diagrams for the two compounds.

DOI: 10.1103/PhysRevB.92.144401 PACS number(s): 75.30.Kz, 75.10.Dg, 75.30.Gw, 75.30.Et

I. INTRODUCTION

Layered oxides of alkali and transition metals are presently being intensively investigated due to their potential applications as electrode materials in modern ionics [1,2], as thermoelectric materials [3,4], and even as superconductors [5,6]. Recently, a lot of attention has been focused on a new generation of layered complex metal oxides with honeycomb-based crystal structure [7–36] with phases such as $A^+{}_3M^{2+}{}_2X^{5+}O_6$ and $A^+{}_2M^{2+}{}_2Te^{6+}O_6$ (A = Li, Na; X = Bi, Sb; and M is a transition metal), where ordered mixed layers of magnetic cations M^{2+} and X^{5+} (or M^{2+} and Te^{6+}) alternate with nonmagnetic alkali metal layers. The crystal structures are very soft, and even slight modification, for example, in a stacking mode of alternating layers, results in drastic changes in the magnetic properties. In turn, increasing the distance between magnetically active layers leads to a weakening of interplanar spin interactions and concomitant possible lowering of the magnetic dimensionality of the systems.

The honeycomb arrangement of cations within the magnetically active layers provides a large variety of quantum ground states. The classical (S = infinity) Heisenberg model on a honeycomb lattice with nearest-neighbor antiferromagnetic exchange coupling J_1 is known to have a Néel ordered ground state (Fig. 1) [37]. Addition of frustrating second and third neighbor interactions J_2 and J_3 as well as quantum corrections leads to a complex phase diagram. Depending on the spin value and signs and ratios J_2/J_1 and J_3/J_1, different types of spin ordering on the honeycomb lattice can be realized, including Néel, zigzag, stripy, and different spiral orders (Fig. 1) [38]. Moreover, it has been experimentally reported that a nonmagnetic ground state can also be achieved on honeycomb lattices in the presence of either lattice distortion or frustration [10–15,30,35]. For example, a spin-gap behavior was found for O3 packing type Cu^{2+} honeycomb compounds $Na_2Cu_2TeO_6$ [10,11], $Na_3Cu_2SbO_6$ [11–15,35], and related delafossite-derived honeycomb $S = 1/2$ compound $Cu_5SbO_6(Cu^+{}_3Cu^{2+}{}_2Sb^{5+}O_6)$ [30]. Antiferromagnetic zigzag ordering in the honeycomb plane was observed recently for the structurally related honeycomb lattice delafossites $Cu_3Ni_2SbO_6$ and $Cu_3Co_2SbO_6$ [31]. No long-range magnetic order was found for honeycomb $Na_3LiFeSbO_6$, Na_4FeSbO_6, and Li_4MnSbO_6, probably due to disorder and frustration effects [34,36]. At the same time, honeycomb lattice O3 type phases $Na_3M_2SbO_6$ (M = Cu, Ni, Co) [17,19,31],

*Corresponding author: zvereva@mig.phys.msu.ru

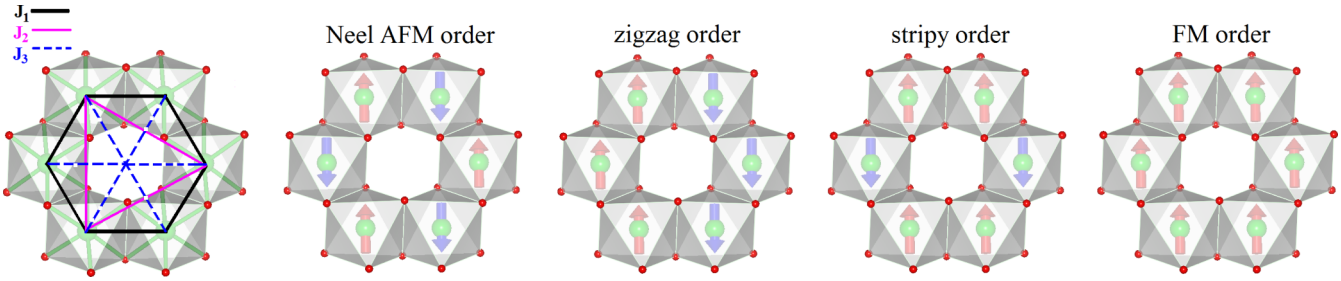

FIG. 1. (Color online) 2D honeycomb lattice Heisenberg model with up to third neighbor exchanges, $J_{1,2,3}$, and spin-configuration diagrams for Néel, zigzag, stripy, and ferromagnetic (FM) order.

$Li_3Ni_2SbO_6$ [20], $Li_3Ni_2BiO_6$ [21], $Na_3Ni_2BiO_6$ [33], as well as P2 type $Na_2M_2TeO_6$ (M = Co, Ni) [18,19], were found to order antiferromagnetically at low temperatures, but their real quantum ground state remains unknown and requires joint experimental and theoretical efforts to be determined. The influence of the interlayer coupling and of the anisotropy on the ground state in such systems is largely unexplored at present.

The present work is devoted to the investigation of new quasi-two-dimensional (2D) honeycomb lattice compounds $Li_3Ni_2SbO_6$ and $Na_3Ni_2SbO_6$. We combine magnetic susceptibility, magnetization, specific heat, electron spin resonance, and nuclear magnetic resonance (NMR) measurements with density functional theory (DFT) calculations and uniquely identify the appropriate magnetic model for these systems as well as the corresponding applied field–temperature phase diagram.

Basic magnetic properties of $Li_3Ni_2SbO_6$ and $Na_3Ni_2SbO_6$ have been reported recently [17,20], but a systematic analysis of their electronic and magnetic behavior is missing. The ordered structure of $Li_3Ni_2SbO_6$ was refined in the space group $C2/m$ [20]. For $Na_3Ni_2SbO_6$, the initial structure determination was complicated by multiple stacking faults, resulting in superposition of different types of superstructure: $C2/m$, $C2/c$, and $P3_112$ [22]. Nevertheless, it was unambiguously shown that the general layout of the structure is the same as in $Li_3Ni_2SbO_6$ [22,17]. Therefore, our analysis of magnetic interactions was based on a $C2/m$ model constructed on lattice parameters and ionic radii sums. Quite recently, the preparation of both ordered and disordered forms of $Na_3Ni_2SbO_6$ was reported [39]. It was confirmed that complete Ni/Sb ordering within each layer exists even in the "disordered" apparently rhombohedral form. The ordered form was refined in the $C2/m$ space group. The final Ni-Ni, Ni-O, and Sb-O distances [39] differ from our initial model only within 0.001–0.004, 0.002–0.009, and 0.012−0.021 Å, respectively. NiO_6 octahedra in $Na_3Ni_2SbO_6$ have rather regular Ni-O distances but a spread of angles between 82.1° and 95.8° [39]. NiO_6 octahedra are only slightly more regular for $Li_3Ni_2SbO_6$, with angles between 83.4° and 94.9° [20]. A general view of the crystal structure and the honeycomb network of octahedrally coordinated nickel ions in $Na_3Ni_2SbO_6$ are shown in Fig. 2.

II. EXPERIMENTAL AND CALCULATION DETAILS

Polycrystalline $Na_3Ni_2SbO_6$ and $Li_3Ni_2SbO_6$ samples were prepared by conventional solid-state reactions at 980–1030 °C followed by quenching as described in Refs. [20,22]. Their phase purity was verified by powder X-ray diffraction (International Centre for Diffraction Data [ICDD] Powder Diffraction Files (PDF) 00-53-0344 and 00-63-566).

Magnetic measurements were performed by means of a Quantum Design Magnetic Property Measurement System (MPMS) XL-7 magnetometer. The temperature dependencies of the magnetic susceptibility were measured at a magnetic field $B = 0.1$ T in the temperature range 1.8–300 K. The magnetic susceptibility data were also taken over the temperature range 1.8–30 K in applied field strengths up to 7 T. The isothermal magnetization curves were obtained in static magnetic fields $B \leqslant 7$ T and at $T \leqslant 20$ K after cooling the sample in zero magnetic field. Magnetic measurements in pulsed magnetic fields were made using the 30 T system with a rise time of about 8 ms in a temperature range 2.4–20 K. For temperatures lower than 4.2 K, the samples were immersed in a pumped bath of liquid helium.

The specific heat measurements were carried out by a relaxation method using a Quantum Design Physical Property Measurement System (PPMS)-9 system. Plate-shaped samples of $Li_3Ni_2SbO_6$, $Na_3Ni_2SbO_6$, and their nonmagnetic analogue $Li_3Zn_2SbO_6$ of ∼0.2 mm thickness and 7.96 mg, 8.5 mg, and 8.6 mg mass, respectively, were obtained by cold pressing of the polycrystalline powder. Data were collected at zero magnetic field and under applied fields up to 9 T in the temperature range 2–300 K.

Electron spin resonance (ESR) studies were carried out using an X-band ESR spectrometer CMS 8400 (ADANI)

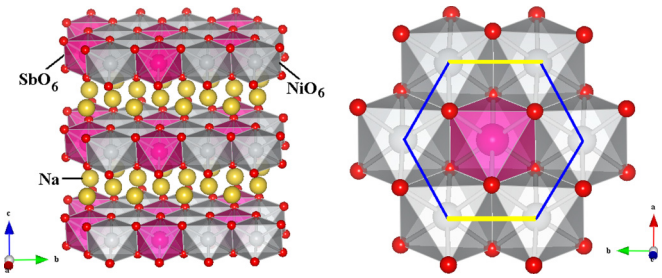

FIG. 2. (Color online) (Left) Polyhedral view of the layered crystal structure of $Na_3Ni_2SbO_6$: the Sb octahedra are shown in pink, Ni octahedra are in gray, Na ions are yellow spheres, and O ions are small red spheres. The octahedra around the Na ions are omitted for simplicity. (Right) A fragment of the $C2/m$ structure of $Na_3Ni_2SbO_6$ in the ab plane (the magnetoactive layers) showing an organization of Ni–O bonds between edge-shared NiO_6 octahedra.

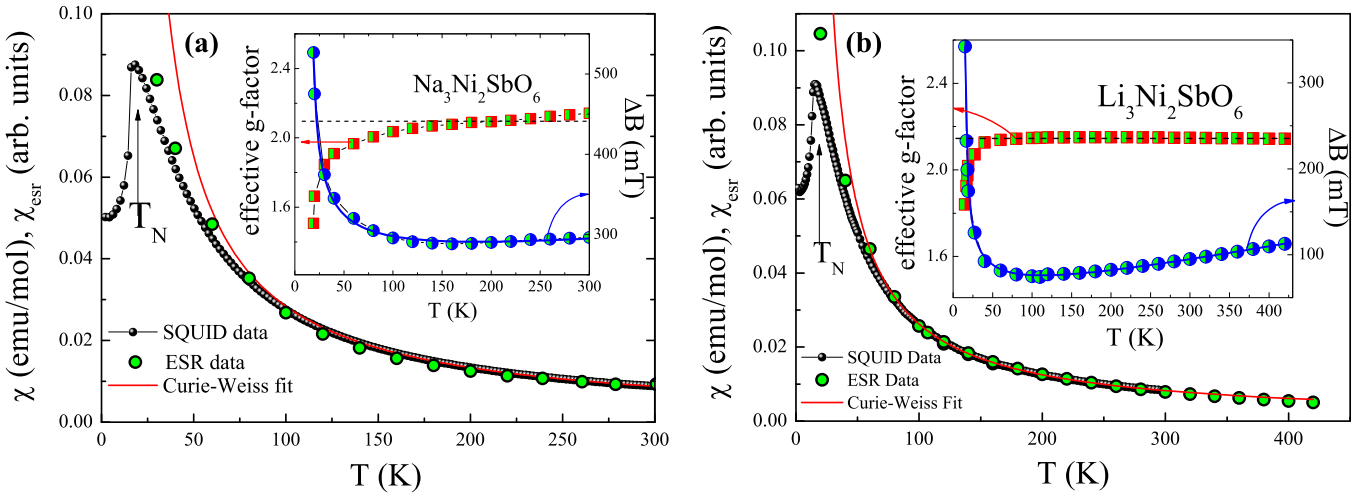

FIG. 3. (Color online) Temperature dependence of the magnetic susceptibility at $B = 0.1$ T (black filled circles) and integral ESR intensity (green circles) for $Na_3Ni_2SbO_6$ (a) and $Li_3Ni_2SbO_6$ (b). The red solid curves represent an approximation in accordance with the Curie-Weiss law. Insets: Temperature dependencies of the effective g factors (half-field squares) and ESR line widths (half-filled circles) for both compounds. The blue solid curves on insets represent the result of fitting in the frame of modified Huber theory as described in the text. SQUID = superconducting quantum interference device.

($f \approx 9.4$ GHz, $B \leqslant 0.7$ T) equipped with a low-temperature mount, operating in the range $T = 6$–470 K. The effective g factors of our samples were calculated with respect to an external reference for the resonance field. We used *a,g*-bisdiphenyline-*b*-phenylallyl (BDPA) with $g_{\mathrm{ref}} = 2.00359$ as a reference material.

The ^{7}Li ($I = 3/2$) and ^{23}Na ($I = 3/2$) NMR spectra of the $Na_3Ni_2SbO_6$ and $Li_3Ni_2SbO_6$ samples were measured on a Tecmag pulse solid-state NMR spectrometer at a frequency of 39.7 MHz. NMR spectra were obtained by point-by-point measuring the intensity of the Hahn echo versus magnetic field. The spin-lattice relaxation time T_1 was measured with the method of stimulated echo.

The electronic structure of $Na_3Ni_2SbO_6$ and $Li_3Ni_2SbO_6$ was calculated within DFT using the full potential local orbital (FPLO) basis set [40] and the generalized gradient approximation (GGA) functional [41]. The $Li_3Ni_2SbO_6$ structure was taken from Ref. [20]. We used a $12 \times 12 \times 12$ **k** mesh to converge energy and charge density. We estimated the magnetocrystalline anisotropy energy (MAE) using fully relativistic GGA calculations in a ferromagnetic spin configuration with a $16 \times 16 \times 16$ **k** mesh. Given the extremely high accuracy required for MAE, the calculations were repeated and corroborated employing a different code, the Vienna *Ab initio* Simulation Package (VASP) package, using projector-augmented wave (PAW) potentials and including self-consistent spin-orbit calculations [42]. We extracted the in-plane exchange couplings by lowering the symmetry from $C2/m$ to $P1$. The exchange couplings were obtained by performing total energy calculations with the GGA and GGA + Hubbard U (GGA + U) functionals and mapping the energy difference of various spin configurations onto a Heisenberg model as described in Refs. [43,44]. For the interplane exchange coupling, we used a $1 \times 1 \times 2$ supercell.

III. RESULTS AND DISCUSSION

A. Magnetic susceptibility

The static and dynamic magnetic properties of $A_3Ni_2SbO_6$ (A = Li, Na) are similar for both samples and are in full agreement with previously reported data [17,20]. The magnetic susceptibility $\chi = M/B$ in weak magnetic fields passes through sharp maxima at $T \sim 15$ and 17 K for Li and Na samples, respectively, and then it drops by about one third (Fig. 3). Such a behavior indicates an onset of antiferromagnetic long-range ordering in the material at low temperature and is typical for polycrystalline easy-axis antiferromagnets.

The high-temperature magnetic susceptibility nicely follows the Curie-Weiss law with addition of a temperature-independent term χ_0:

$$\chi = \chi_0 + \frac{C}{T - \Theta} \tag{1}$$

where Θ is the Weiss temperature, and C is the Curie constant $C = N_A \cdot {\mu_{\mathrm{eff}}}^2 \cdot {\mu_B}^2/3k_B$, where N_A is Avogadro's number, μ_{eff} is the effective magnetic moment, μ_B is Bohr's magneton, and k_B is Boltzmann's constant. The best fitting according to Eq. 1 in the range 200–300 K resulted in positive $\chi_0 \sim 1 \times 10^{-4}$ emu/mol, which appears to indicate a predominance of the Ni^{2+} van Vleck paramagnetic contribution over diamagnetic contributions. Our analysis yields positive values for the Weiss temperature: ~8 K for the Li sample and ~12 K for the Na sample, respectively, suggesting the existence of nonnegligible ferromagnetic couplings, although the system orders antiferromagnetically at low temperatures. The effective magnetic moments determined from the corresponding Curie constants were found to be 4.3 and 4.4 μ_B/f.u. for $Li_3Ni_2SbO_6$ and $Na_3Ni_2SbO_6$, respectively, where f.u. is formula units. These values agree well with theoretical estimates ${\mu_{\mathrm{theor}}}^2 = g^2{\mu_B}^2 nS(S+1)$, where n is number of Ni^{2+} ions per formula unit, using an effective g value ~2.15

and assuming Ni^{2+} in a high-spin configuration ($S = 1$). In an applied magnetic field, the maximum of the magnetization $M(T)$ broadens (not shown) and slightly shifts toward low temperatures with increasing magnetic field, as one would expect in the presence of antiferromagnetic ordering.

B. Electron spin resonance

ESR data in the paramagnetic phase ($T > T_N$) show a single broad Lorentzian shape line ascribable to Ni^{2+} ions in octahedral coordination. The main ESR parameters (effective g factor, the ESR line width, and the integral ESR intensity) were deduced by fitting the experimental spectra with an asymmetric Lorentzian profile [45], taking into account a small contribution of the dispersion into the absorption and two circular components of the exciting linearly polarized microwave field on both sides of $B = 0$,

$$\frac{dP}{dB} \propto \frac{d}{dB}\left[\frac{\Delta B + \alpha(B - B_r)}{\Delta B^2 + (B - B_r)^2} + \frac{\Delta B - \alpha(B + B_r)}{\Delta B^2 + (B + B_r)^2}\right] \quad (2)$$

where P is the power absorbed in the ESR experiment, B is the magnetic field, B_r is the resonance field, and ΔB is the line width. Here, α denotes the asymmetry parameter, which is the fraction of the dispersion added to the absorption. The admixture of dispersion to the absorption signal is usually observed in metals. Here, we are dealing with an insulator, in which the asymmetry arises from the influence of nondiagonal elements of the dynamic susceptibility. This effect is often observed in systems with interactions of low symmetry, geometrical frustration, and sufficiently broad resonance lines ($B_r \approx \Delta B$) [46–49].

The overall temperature behavior of the ESR parameters agrees very well for both samples. The integral ESR intensity χ_{esr}, which is proportional to the number of magnetic spins, was estimated by double integration of the first derivative ESR spectrum dP/dB. It is shown in Fig. 3 along with static susceptibility data for comparison. One can see that χ_{esr} follows the Curie-Weiss relationship and agrees well with the behavior of χ for both compounds. The average effective g factor, $g = 2.15 \pm 0.03$, remains almost temperature independent in the paramagnetic phase down to ~140 K for the Na sample and ~70 K for the Li sample, and then the visible shift of the resonant field to higher magnetic fields begins upon approaching the Néel temperature. This behavior implies the presence of strong short-range correlations in the compound at temperatures noticeably higher than T_N, which is frequently characteristic of systems with a frustration and lower dimensionality [50,51]; the range of these correlations is apparently wider for the Na sample. Remarkably, the ESR signal for the $Na_3Ni_2SbO_6$ sample is at least twice as broad compared to that for $Li_3Ni_2SbO_6$ (insets in Fig. 3), and as a consequence, the asymmetry parameter takes an appreciable value $\alpha \sim 0.4$ for the Na compound, while it is negligibly small, $\alpha \sim 0$, for the Li sample. Note, that the value $\alpha = 0$ leads to a symmetric Lorenzian line, whereas the value $\alpha = 1$ gives an asymmetric resonance line with absorption and dispersion at equal strength.

The line width decreases weakly and almost linearly upon lowering of the temperature, passes through a minimum at ~140 K for the Na sample and ~120 K for the Li sample, and eventually changes the trend. Upon further decrease of the temperature, the absorption line broadens significantly, and the ESR signal vanishes in the vicinity of the Néel temperature, indicating an opening of an energy gap for resonance excitations, e.g., due to the establishment of antiferromagnetic order. The broadening of the ESR line may be treated in terms of the critical behavior of ESR line width due to slowing down of spin fluctuations in the vicinity of an order-disorder transition [52–55]. This causes the divergence of the spin correlation length, which in turn affects the spin-spin relaxation time of exchange-narrowed ESR lines, resulting in the critical broadening. To account for the ΔB behavior over the whole temperature range, we have also included a third linear term into the fitting formula:

$$\Delta B(T) = \Delta B^* + A \cdot \left[\frac{T_N^{ESR}}{T - T_N^{ESR}}\right]^{\beta} + C \cdot T \quad (3)$$

where the first term ΔB^* describes the exchange-narrowed line width, which is temperature independent, while the second term reflects the critical behavior, with T_N^{ESR} being the temperature of the order-disorder transition, and β representing the critical exponent. Solid blue lines in insets on Fig. 3 represent a least-squares fit of the $\Delta B(T)$ experimental data in accordance with Eq. 3. The best fit was obtained with the parameters listed in Table I.

TABLE I. The parameters yielded from fitting of temperature dependencies of the ESR line width ΔB in accordance with Eq. (3) for $Na_3Ni_2SbO_6$ and $Li_3Ni_2SbO_6$.

	T_N^{ESR} (K)	ΔB^* (mT)	A (mT)	C (mT/K)	β
$Na_3Ni_2SbO_6$	15 ± 1	230 ± 5	130 ± 5	0.12	0.5 ± 0.1
$Li_3Ni_2SbO_6$	13 ± 1	25 ± 5	95 ± 5	0.18	0.8 ± 0.1

Here, it is worth mentioning two important issues following from the analysis of the line-width behavior. First, the main experimental feature of the ΔB temperature evolution is that the line width passes through a minimum as T is decreased. This is to be contrasted with the behavior of a three-dimensional (3D) system, where the line width usually varies approximately as $\Delta B(T) \sim (\chi T)^{-1}$, achieving the temperature-independent high-temperature limit ΔB^* associated with the contribution of anisotropic spin-spin interactions in an exchange-narrowed regime, since in three dimensions the sum over all wave vectors $\mathbf{q}$ tends to be weakly dependent on T [56]. At the same time, as it has been shown by Richards and Salamon [56], if most of the contribution comes from $\mathbf{q} = 0$, as is the case in 2D, one should expect $\Delta B(T) \sim (\chi T)$. Moreover, since the relative strength of $\mathbf{q} \approx 0$ modes decreases with lowering temperature, it follows that the anisotropy will also decrease. Indeed, such behavior was experimentally observed in many 2D antiferromagnets [57–65], and the linear dependence of ΔB was usually associated either with a phonon modulation of the anisotropic and antisymmetric exchange interactions, with a dependence proportional to the intralayer exchange parameter J^4, or with the crystalline field, the latter in the $S > 1/2$ case. For transition metals where the orbital contribution to the ground state is severely quenched, the latter interactions are rather small and give rise to $d(\Delta B)/dT$ usually smaller or

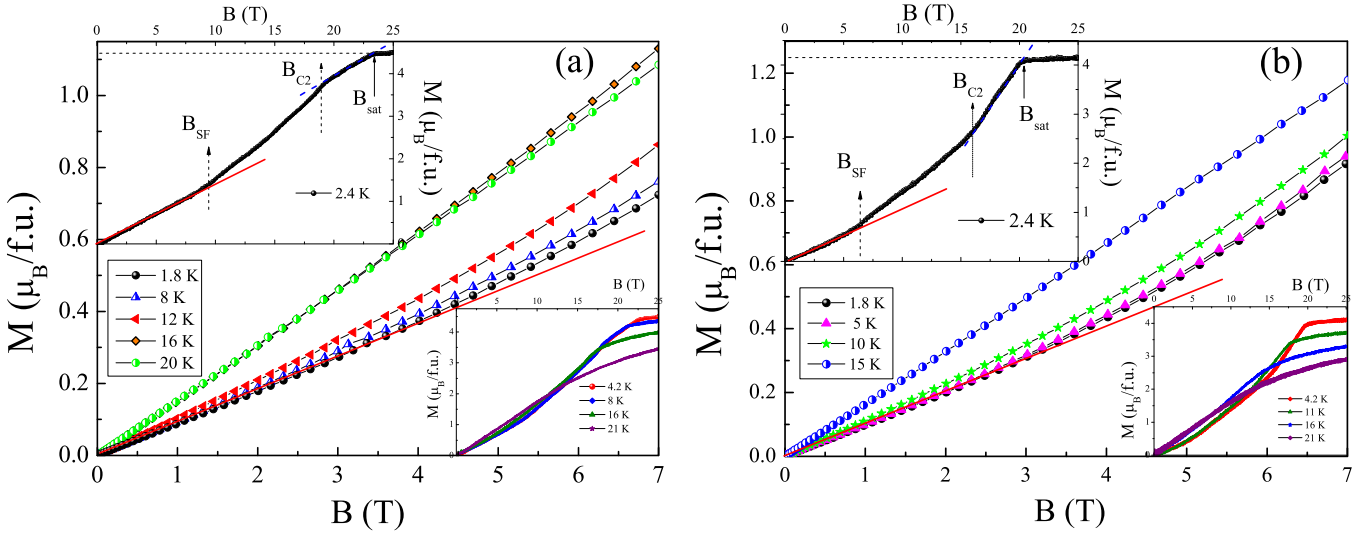

FIG. 4. (Color online) The magnetization isotherms in static and pulsed (insets) magnetic fields for $Na_3Ni_2SbO_6$ (a) and $Li_3Ni_2SbO_6$ (b) at various temperatures. Arrows point to the positions of the field-induced phase transitions.

equal to 0.1 mT/K. In the present case, however, the rate is a bit larger, indicating the noticeable role of the orbital contribution for Ni^{2+} ions.

The second point to note is that in the framework of Kawasaki's approach [52,53], the absolute value of the critical exponent can be expressed as $\beta = [(7+\eta)\nu/2 - 2(1-\zeta)]$, where ν describes the divergence of correlation length, η is a critical exponent for the divergence of static correlations, and ζ reflects the divergence of the specific heat. Using the values $\eta = \zeta = 0$ and $\nu = 2/3$ for 3D antiferromagnets in the framework of the Heisenberg model, β becomes $1/3$, which is obviously lower than our experimental values.

Both the above mentioned conclusions, following from the analysis of spin dynamics, support the picture of the 2D character of magnetic correlations in $Na_3Ni_2SbO_6$ and $Li_3Ni_2SbO_6$ compounds and are compatible with a spin-configuration model, which we suggest based on DFT calculations (see below).

C. Magnetization

The magnetization isotherms M(B) in static up to 7 T and in pulsed up to 25 T magnetic fields for $Na_3Ni_2SbO_6$ and $Li_3Ni_2SbO_6$ at various temperatures are presented in Fig. 4. We observe that the full saturation of the magnetic moment is achieved at about $B_{sat} \sim 23$ and 20 T for $Na_3Ni_2SbO_6$ and $Li_3Ni_2SbO_6$, respectively, and M_{sat} is in good agreement with the theoretically expected saturation magnetic moment for two high-spin Ni^{2+} ions ($S = 1$) per formula unit assuming a state: $M_s = 2\,g S \mu_B = 4.3\,\mu_B$/f.u. (see upper insets in Fig. 4). In addition, the magnetization curves demonstrate a clear upward curvature, suggesting the presence of a magnetic field–induced spin-flop type transition in the compounds with critical fields $B_{SF} \sim 9.8$ and 5.5 T for $Na_3Ni_2SbO_6$ and $Li_3Ni_2SbO_6$, respectively. Moreover, further increase of the magnetic field leads to another change in curvature of the magnetization curves at about $B_{C2} \sim 18$ for $Na_3Ni_2SbO_6$ and $B_{C2} \sim 15$ T for $Li_3Ni_2SbO_6$, indicating the presence of one more magnetic field–induced phase transition, which is perhaps related to additional spin reorientation in applied fields. With increasing temperature, both B_{SF} and B_{C2} anomalies slightly shift to lower fields, weaken in amplitude, and eventually disappear above the Néel temperature T_N (see lower insets in Fig. 4). Similar behavior was reported for several other structurally related honeycomb compounds recently. In particular, two spin-reorientation transitions below the Néel temperature were revealed for $Na_3Ni_2BiO_6$ [33] and for both 2H and 3R polytypes of $Cu_3Co_2SbO_6$ [31,66]. Remarkably, the magnetic structure as refined experimentally from low-temperature neutron diffraction studies was described as alternating ferromagnetic chains coupled antiferromagnetically, giving overall antiferromagnetic zigzag alignment for both $Na_3Ni_2BiO_6$ (with propagation vector $\mathbf{q} = [010]$) and the 2H polytype of $Cu_3Co_2SbO_6$ (with propagation vector $\mathbf{q} = [100]$).

D. Specific heat

In order to analyze the nature of the magnetic phase transition and to evaluate the corresponding contribution to the specific heat and entropy, the structurally similar [7] diamagnetic material $Li_3Zn_2SbO_6$ has been synthesized. The specific heat data for both magnetic and diamagnetic samples in the T range 2–300 K are shown in Fig. 5. The Dulong-Petit value reaches $3Rz = 299$ J/(mol K), with the number of atoms per formula unit $z = 12$. The $C(T)$ data for $A_3Ni_2SbO_6$ (A = Li, Na) in zero magnetic field are in good agreement with the temperature dependence of the magnetic susceptibility in weak magnetic fields, and they demonstrate a distinct λ-shaped anomaly, which is characteristic of a 3D magnetic order (Fig. 5). Note, that the absolute value of the Néel temperature, $T_N \sim 14$ K and 16 K for $Li_3Ni_2SbO_6$ and $Na_3Ni_2SbO_6$, respectively, deduced from $C(T)$ data at $B = 0$ T is slightly lower than the T_{max} in $\chi(T)$ at $B = 0.1$ T (Fig. 3), whereas it correlates well with a maximum on the magnetic susceptibility derivative $\partial\chi/\partial T(T)$. Indeed, as has been shown by Fisher [67,68], the temperature dependence of the specific heat $C(T)$ for antiferromagnets with short-range interactions should follow the derivative of the magnetic susceptibility in

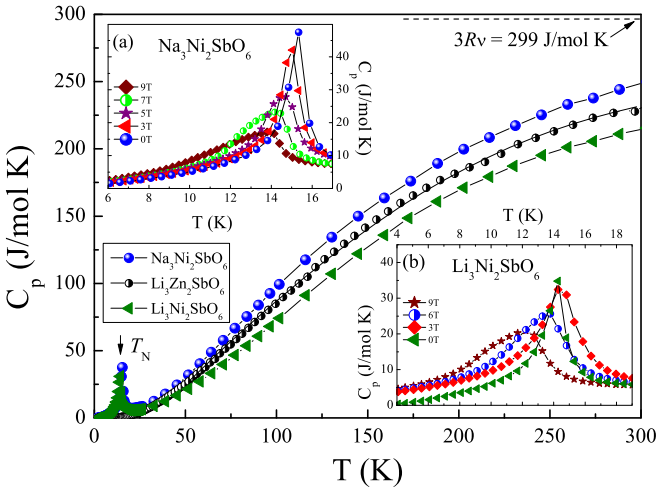

FIG. 5. (Color online) Temperature dependence of the specific heat in $Li_3Ni_2SbO_6$ (green triangles), $Na_3Ni_2SbO_6$ (blue filled circles), and their nonmagnetic analogue $Li_3Zn_2SbO_6$ (black half-filled circles) in zero magnetic field. Insets: Enlarged low-temperature parts highlight the onset of antiferromagnetic spin ordering and shift of T_N in magnetic fields.

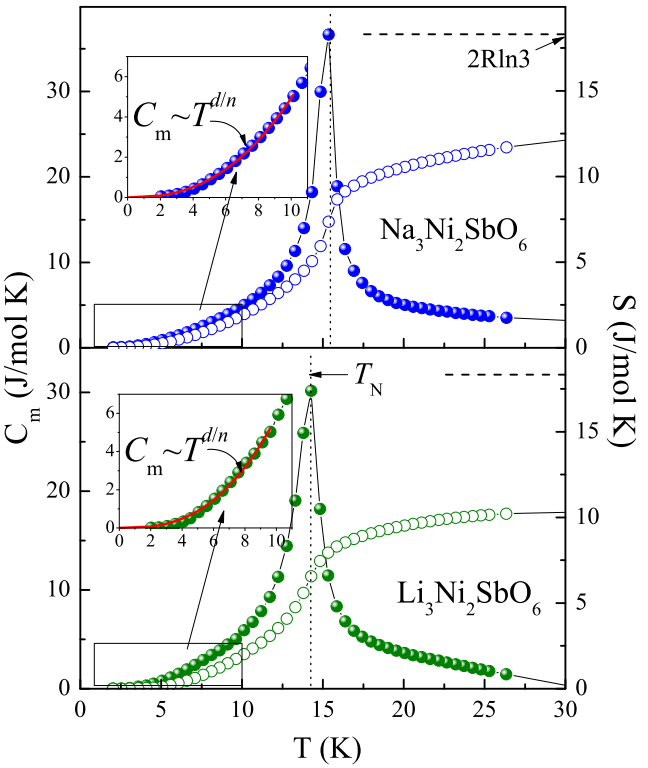

FIG. 6. (Color online) Magnetic specific heat (filled circles) and magnetic entropy (open circles) for $A_3Ni_2SbO_6$ at $B = 0$ T. Insets: Enlarged low-temperature parts with solid curve indicating the spin-wave contribution estimated in accordance with a $C_m \propto T^{d/n}$ power law for magnons.

accordance with:

$$C(T) = A(\partial/\partial T)[T\chi_{||}(T)] \tag{4}$$

where the constant A depends weakly on temperature. In accordance with Eq. (4), the λ-type anomalies observed in the $C(T)$ dependence at the antiferromagnetic transition temperature are defined by an infinite positive gradient on the curve $\chi_{\|}(T)$ at T_N, while a maximum of $\chi_{\|}(T)$ usually lies slightly above the ordering temperature. Thus, the anomaly in the specific heat should correspond to the similar anomaly in $\partial\chi_{\|}/\partial T(T)$ [69].

We observe a specific heat jump at T_N $\Delta C_p \sim 32$ J/(mol K) and 33 J/(mol K) for $Li_3Ni_2SbO_6$ and $Na_3Ni_2SbO_6$, respectively, which are only slightly smaller than the value expected from the mean-field theory for the antiferromagnetic ordering of two Ni^{2+} ions system assuming all spins to be in the high-spin ($S = 1$) state [70]: $\Delta C_p = 5R\frac{2S(S+1)}{S^2+(S+1)^2} \approx 33.2$ J/(mol K), where R is the gas constant $R = 8.31$ J/(mol K). In applied magnetic fields, the T_N anomaly is rounded and markedly shifts to lower temperatures (see insets in Fig. 5).

For quantitative estimations, we assume that the specific heat of the isostructural compound $Li_3Zn_2SbO_6$ provides a proper estimation for the pure lattice contribution to specific heat. In the frame of the Debye model, the phonon specific heat is described by the function [70]:

$$C_{ph} = 9R\left(\frac{T}{\Theta_D}\right)^3 \int_0^{T/\Theta_D} \frac{e^x x^4}{(e^x-1)^2} dx \tag{5}$$

where $x = \hbar\omega/k_BT$, $\Theta_D = \hbar\omega_{max}/k_B$ is the Debye temperature, ω_{max} is the maximum frequency of the phonon spectrum, and k_B is the Boltzmann constant. The value of the Debye temperature Θ_D estimated from approximating $C(T)$ to this T^3 law in the low-temperature range for the diamagnetic compound $Li_3Zn_2SbO_6$ was found to be about $\sim 515 \pm 5$ K. Normalization of the Debye temperatures has been made taking into account the difference between the molar masses for Zn–Ni and Li–Na atoms in the $A_3Ni_2SbO_6$ compounds, resulting in $\Theta_D \sim 523 \pm 5$ K and 415 ± 5 K for Li and Na samples, respectively.

The magnetic contribution to the specific heat was determined by subtracting the lattice contribution using the data for the isostructural [7] nonmagnetic analogue (Fig. 6). We examine the $C_m(T)$ below T_N in terms of the spin-wave approach, assuming that the limiting low-temperature behavior of the magnetic specific heat should follow a $C_m \propto T^{d/n}$ power law due to magnon excitations [50], where d stands for the dimensionality of the magnetic lattice, and n is defined as the exponent in the dispersion relation $\omega \sim \kappa^n$. For antiferromagnetic (AFM) and ferromagnetic (FM) magnons, $n = 1$ and $n = 2$, respectively. The least-square fit of the data below T_N (insets in Fig. 6) agrees well with $d = 3$ and $n = 1$ for both Li and Na samples, which corroborates the picture of 3D AFM magnon excitations at low temperatures.

In Fig. 6, we also show the entropy change (open circles) in both materials calculated using the equation: $\Delta S_m(T) = \int_0^T \frac{C_m(T)}{T} dT$. We observe that the magnetic entropy ΔS_m saturates at temperatures higher than 25 K, reaching approximately 10–12 J/(mol K). This value is definitely lower than the magnetic entropy change expected from the mean-field theory for a system of two Ni magnetic ions with $S = 1$: $\Delta S_m(T) = 2R\ln(2S+1) \approx 18.3$ J/(mol K). One should

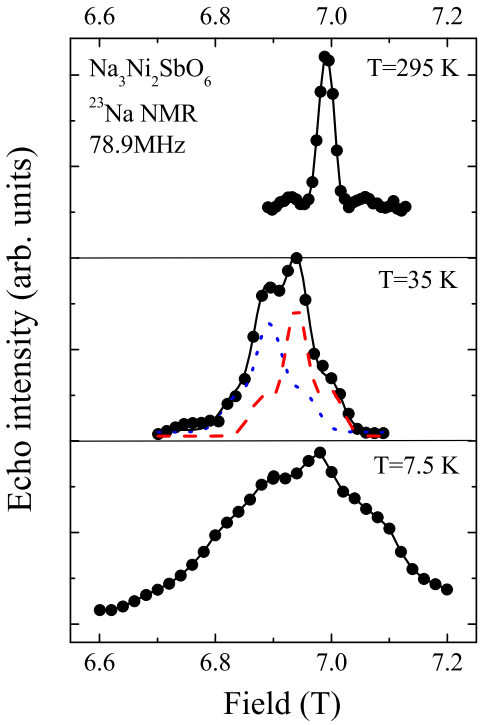

FIG. 7. (Color online) The ^{23}Na NMR spectrum at various temperatures. Dashed lines are the fitted contributions of two Na sites; solid line is the best fit of the spectra.

note that the magnetic entropy released below T_N removes less than 40% of the saturation value. This indicates the presence of appreciable short-range correlations far above T_N, which are usually characteristic features for materials with lower magnetic dimensionality [50,70].

E. Nuclear magnetic resonance

The typical ^{23}Na field-dependent NMR spectrum of $Na_3Ni_2SbO_6$ at room temperature contains a narrow main line and quadrupole satellites (Fig. 7). Upon decreasing the temperature, the spectrum broadens noticeably and shifts to the lower field side. The temperature behavior of the spectrum of $Li_3Ni_2SbO_6$ (not shown) is similar to the data for $Na_3Ni_2SbO_6$. However, the quadrupole moment of Li nuclei is almost 10 times smaller than Na, so that the room-temperature spectrum of $Li_3Ni_2SbO_6$ does not contain the well-resolved satellites.

Both spectra of $Na_3Ni_2SbO_6$ and $Li_3Ni_2SbO_6$ are inhomogeneously broadened and consist of two components, which can be attributed to two crystallographically [20,39] and magnetically nonequivalent positions of alkali metal ions. An example of the spectrum decomposition in $Na_3Ni_2SbO_6$ in accordance with the two resolved components is shown in the middle panel of Fig. 7.

The temperature dependencies of the line shift and line width of Na and Li signals are collected in Fig. 8. Obviously, their behavior agrees well with the corresponding evolution of the magnetic susceptibility below ~200 K.

The low-temperature behavior of the NMR spectrum is caused by the interaction with the magnetic Ni^{2+} ions and reflects the dynamics of the magnetic subsystem. The facts that the shift and broadening of the lines start at much higher temperatures than T_N indicate the existence of strong low-dimensional (short-range) correlations in the magnetic subsystem [50,71]. The slowing down of the Ni magnetic moment fluctuations caused by competing ferromagnetic and antiferromagnetic interactions in the planes with much weaker interplane couplings, as determined from DFT calculations (see next subsection), creates a nonzero average magnetic field at the Na/Li nuclei situated in between the Ni–Sb planes.

The hyperfine tensor value is different for different Na/Li positions, and hence it can explain the different values of Knight shifts and line widths of the spectral components. Another possible explanation of the asymmetric shape of powder NMR spectra, i.e., strong hyperfine tensor asymmetry, seems to us less probable because the ratio of the intensity of the components in both compounds is about 1:1, and the spectrum does not fit to the typical powder line shape. One should mention that the ESR data do not give evidence for the existence of a strong g-factor anisotropy, which also could contribute to the anisotropy of the average field on the position of the alkali metals' nuclei. Nevertheless, the ESR absorption line for the Na compound was found to be essentially wider than for the Li compound, which indicates larger anisotropy

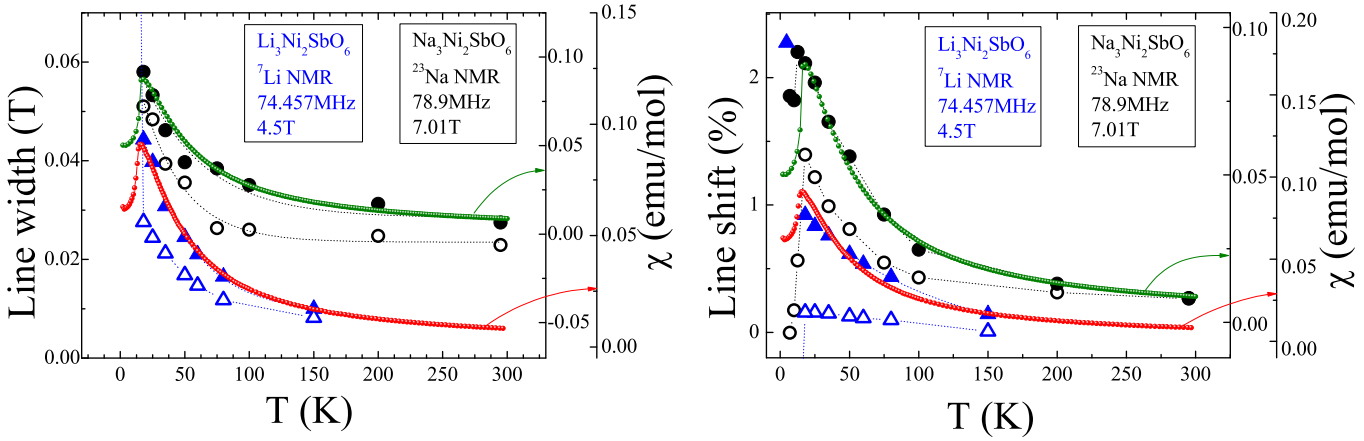

FIG. 8. (Color online) The temperature dependencies of line width (left) and line shift (right) of two components of ^{7}Li (triangles, blue online) and ^{23}Na (circles, black online) NMR signals. Dotted lines are guides for the eye. Small red and green circles are the magnetic susceptibility curves.

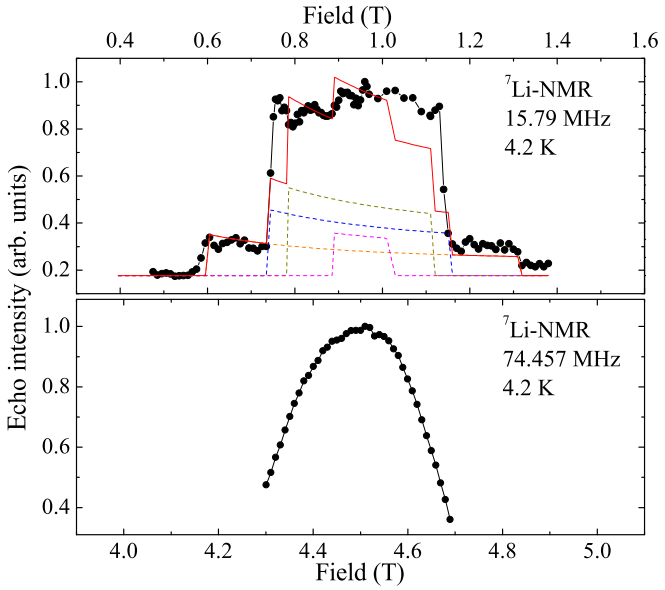

FIG. 9. (Color online) The ^{7}Li spectrum for $Li_3Ni_2SbO_6$ at 4.2 K in antiferromagnetic phase at different magnetic fields: 0.95 T for upper panel and 4.5 T for lower panel. Red line is the result of dipole-dipole calculations; dashed lines are the calculated contributions of different magnetically nonequivalent Li positions in the frame of the powder averaging of the zigzag model.

for the Na compound. It is worth noting that both the NMR line shift and the NMR line width for $Na_3Ni_2SbO_6$ are also markedly larger than for $Li_3Ni_2SbO_6$, even taking into account the field dependence of the inhomogeneously broadened NMR line. This fact is likely to manifest the features of the two different magnetic subsystems of these compounds: The ionic radius of Na is essentially larger than the Li one and leads to enlarged distances between the magnetically active (Ni_2SbO_6) layers and as a consequence to a weaker exchange coupling between them in $Na_3Ni_2SbO_6$.

The NMR line shape of the Na and Li spectra undergoes significant changes upon approaching the Néel temperatures (at about $T \sim 17$ K and $T \sim 15$ K for Na and Li compounds, respectively), indicating the onset of long-range magnetic order when the sublattice of Ni magnetic ions creates a static local field at the alkali metal positions. Na/Li positions are almost symmetrical relative to the two magnetic honeycomb planes. In such cases, the magnitude of the local field is small enough [72], and the total width of the spectra is about 0.2–0.35 T, depending on the external magnetic field.

We should note that the external magnetic field range in both cases (4.5 T for ^{7}Li and 7.01 T for ^{23}Na) corresponds to the development of the spin-flop phase (compare with B_{SF} values, which are about 5.5 T and 9.8 T for $Li_3Ni_2SbO_6$ and $Na_3Ni_2SbO_6$ as described above). The differences in the internal field distribution and magnitude at different magnetic fields are exemplified by the NMR spectrum of ^{7}Li (Fig. 9) obtained in relatively large (4.5 T) and small (0.95 T) external fields.

The local fields on the Li positions at the external field $B = 0.95$ T were calculated in the frame of the dipole-dipole model assuming an isotropic hyperfine tensor [73]. The quadrupole splitting and inhomogeneous line broadening were not taken into account. The calculation included 16 nearest-neighbor Ni ions in a sphere of radius 5.2 Å, and the powder averaging of the internal magnetic field was made according to Ref. [74]. A similar approach has been successfully used before for NMR spectra simulation in other low-dimensional systems [see, for example, Refs. [75,76]]. The calculations in the frame of different spin-configuration models, mentioned in Fig. 1, lead to a conclusion that most parts of these models are inappropriate to account for the shape of the experimental spectrum. The calculated spectrum, which reproduces fairly well the experimental result, was obtained only assuming a zigzag spin structure with spins oriented perpendicular to the plane (as shown by a red solid curve in Fig. 9).

For this spin structure, the calculations in a small external field limit yield four magnetically nonequivalent Li positions contributing to the spectrum in the antiferromagnetic phase, subject to four different values of the internal magnetic field consistent with two crystallographically nonequivalent Li positions. It is worth noting that the Li positions with a minimal internal (local) field (the narrowest contribution on Fig. 9) are likely to be the most affected by the small changes in the spin configuration. Since the external field (~ 1 T) applied in the experiment was about 1/5 of the B_{SF} value, one could expect that the Ni spins in AF sublattices are already slightly canted, resulting in larger local field on these fourth Li positions than the one calculated in a small external field limit. So the spectral contribution of this Li site should be broader and thus more intensive than is suggested by the present simulation. This difference in the widths of spectral components explains the apparent lack of intensity from this fourth Li position in our fit. The small external field limit dipole-dipole simulation is rather simplified; nevertheless, it indicates that a zigzag spin structure is the most favorable ordered state in $Li_3Ni_2SbO_6$ at low fields.

At 4.5 T, we have a smooth spectrum shape due to the partial flipping of the spins while the spin-flop phase develops. The proper fitting of the 4.5 T spectrum was impossible because the spin-flop transition does not occur at that field (as was mentioned above, $B_{SF} \sim 5.5$ T for the Li sample). However, on the basis of our calculations, one can expect a comparably narrow rectangular-like spectrum in the spin-flop phase. To verify the magnetic structure in the spin-flop phase, high-field NMR experiments may be useful, but they were beyond of the scope of this work. In the next section, we show that the critical field, at which the spin-flop phase appears, agrees reasonably with DFT estimations.

F. DFT determination of exchange interactions

In Fig. 10, we present the electronic structure of $Na_3Ni_2SbO_6$ in the GGA in the energy range [−2 eV, 0.5 eV] around the Fermi level. There are ten bands of predominant Ni character, originating from the 3*d* bands of the two Ni ions in the primitive cell used for the calculation. This band manifold is 4/5th filled, since in $Na_3Ni_2SbO_6$ Ni is in the Ni^{2+} ($3d^8$) oxidation state, and Sb is in the Sb^{5+} state (filled shell). The distorted octahedral environment of Ni, NiO_6, leads to a t_{2g}–e_g splitting of about 1.5 eV. The three t_{2g} states $3d_{xy}$, $3d_{yz}$, and $3d_{xz}$ are completely filled (see the density of states [DOS]), and the e_g states $3d_{z2}$ and $3d_{x2\text{-}y2}$ are half-filled. Thus, we expect Ni to be in a high-spin state with $S = 1$ in $Na_3Ni_2SbO_6$. Indeed, spin-polarized GGA calculations show that Ni favors

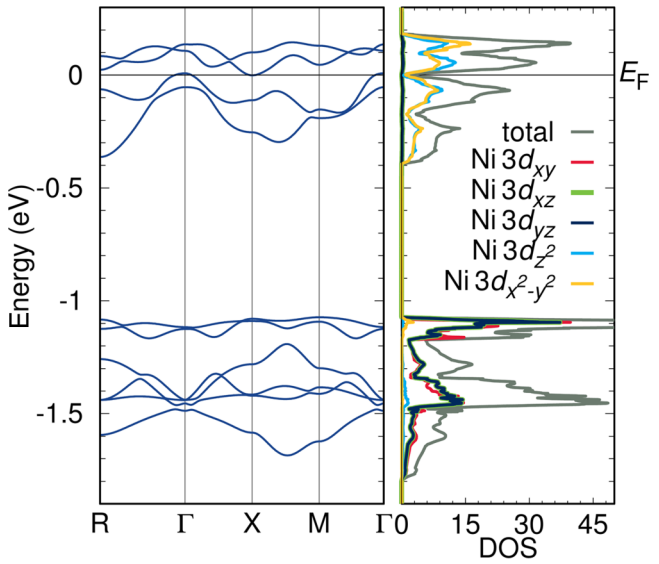

FIG. 10. (Color online) Band structure and DOS of $Na_3Ni_2SbO_6$. Partial densities of states for the Ni $3d$ orbitals are also shown.

moments of 2 μ_B for both compounds. The electronic structure of $Li_3Ni_2SbO_6$ (not shown) is similar to that of $Na_3Ni_2SbO_6$.

Both systems are insulators, and consideration of the zigzag magnetic order in the calculations opens a gap in the electronic structure of about 1.5 eV. Including correlation effects as implemented in GGA + U and for a value of U–J = 4 eV, which is reasonable for $3d$ electrons, we obtain a charge gap of 2.77 eV. A refinement of this choice will be discussed below. Measurements of the charge gap will be desirable but are beyond the scope of the present work.

We now proceed to analyze the magnetic interactions in $Na_3Ni_2SbO_6$ and $Li_3Ni_2SbO_6$. In order to obtain the magnetic couplings, we performed total energy calculations for different spin configurations within GGA and GGA + U and mapped their differences to a Heisenberg model. Total energy differences between spin configurations for the four Ni sites in the conventional unit cell with symmetry lowered to $P1$ yield the first three exchange couplings given in Table II for $Na_3Ni_2SbO_6$ (converged on an 8 × 8 × 8 **k** mesh). J_3 is a second nearest-neighbor coupling within the hexagon and turns out to be quite small. The nearest-neighbor coupling J_1 is antiferromagnetic and strongly depends on the value of U in the GGA + U calculation. The next nearest-neighbor coupling, J_2, is ferromagnetic and is nearly independent of U. The pattern is shown in Fig. 11. The ratio $|J_1/J_2|$ thus depends on which U better describes the material. As mentioned above, the average charge gap at U–J = 4 eV is 2.77 eV; at U–J = 6 eV, it is 2.96 eV. We note that the

TABLE II. Exchange couplings of $Na_3Ni_2SbO_6$ and $Li_3Ni_2SbO_6$ (in Kelvin) calculated with GGA + U at U = 5.5 eV, J = 1 eV. J_3 is a second-nearest-neighbor coupling across a hexagon; J_5 is a coupling along c between the honeycomb layers.

	J_1 (K)	J_2 (K)	J_3 (K)	J_5 (K)
$Na_3Ni_2SbO_6$	15	−22	0	1
$Li_3Ni_2SbO_6$	18	−25	0	2

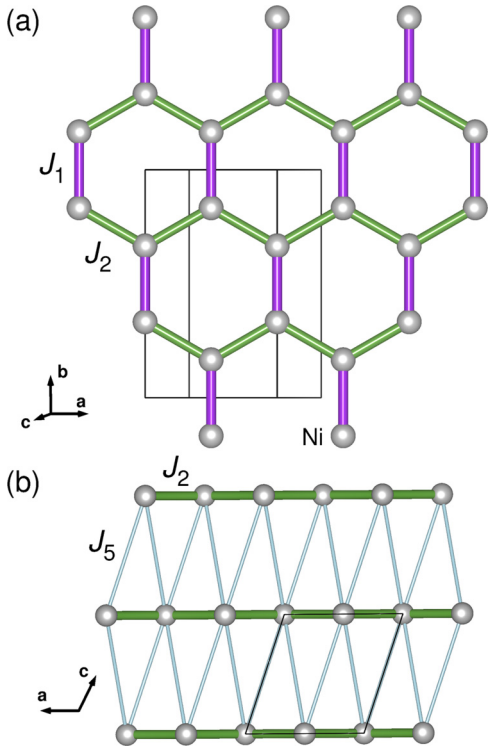

FIG. 11. (Color online) Important exchange paths of $Na_3Ni_2SbO_6$. (a) The purple nearest-neighbor coupling J_1 is antiferromagnetic; the green next-nearest-neighbor coupling J_2 is ferromagnetic. (b) There is a small antiferromagnetic coupling J_5 between the honeycomb Ni planes (light blue).

present calculations clearly favor a zigzag magnetic order of Ni; the zigzag magnetic order also has the lowest energy of all four spin configurations considered. Zigzag order is 2.4 meV per formula unit lower in energy than ferromagnetic order at U–J = 4.5 eV. A 1 × 1 × 2 supercell was used to estimate the order of magnitude of interlayer exchange couplings and is given as J_5 [77] in Table II. In order to decide which value of U is the best for $Na_3Ni_2SbO_6$ and $Li_3Ni_2SbO_6$, we calculated the magnetic susceptibilities using tenth-order high-temperature series expansion (HTE10) [78]. From comparison with the experimental susceptibility in Fig. 3, we have found that U–J = 4.5 eV is the best choice. The corresponding set of the exchange couplings for $Li_3Ni_2SbO_6$ is also given in Table II. Note that due to the smaller interlayer distance in $Li_3Ni_2SbO_6$, the order of nearest-neighbor distances is reversed.

Thus, the present DFT results allow us to compare the magnetic Hamiltonians of $Na_3Ni_2SbO_6$ and $Li_3Ni_2SbO_6$. The intralayer couplings J_1 and J_2 are slightly larger in the Li system than in the Na system due to the shorter Ni−Ni distances in the Li system. The most significant difference is the slightly more 3D character of $Li_3Ni_2SbO_6$ as seen in the somewhat larger interlayer couplings. This is plausible because the smaller Li ions lead to a smaller c lattice parameter and thus a smaller separation between the honeycomb layers.

Finally, we have performed fully relativistic spin-polarized calculations for $Na_3Ni_2SbO_6$ in order to estimate the importance of spin-orbit coupling and determine the easy axis for the Ni spins and the corresponding magnetocrystalline anisotropy.

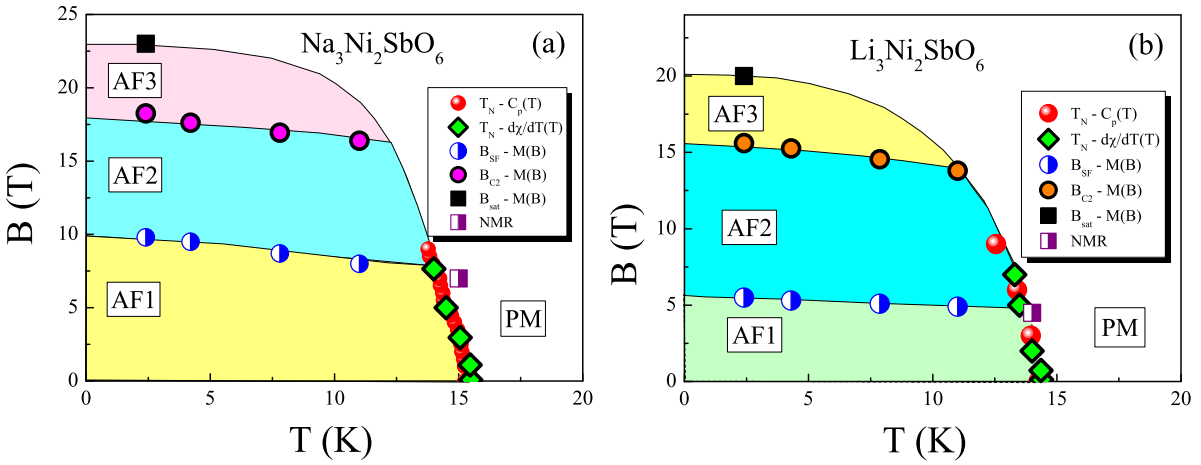

FIG. 12. (Color online) Magnetic phase diagrams for antimonates $A_3Ni_2SbO_6$: (a) A = Na; (b) A = Li.

We have found that the lowest energy is obtained by orienting the quantization axis along c^*, perpendicular to the honeycomb layers. In-plane energies are 0.067 meV/f.u. (a axis) and 0.072 meV/f.u. (b axis) higher in energy. This estimate agrees with the calculated anisotropy energies using VASP: We obtain in-plane energies 0.088 meV/f.u. (a axis) and 0.065 meV/f.u. (b axis) higher than the out-of-plane case. Therefore, the spins tend to align perpendicular to the honeycomb layers, in agreement with the suggestion from NMR experiments (see previous section).

Using the approximation of Ref. [79], we estimate the value of the spin-flop field B_{SF} as $B_{SF} = 2\sqrt{K\Delta}/M$, where K is the magnetocrystalline anisotropy energy, $\Delta = 2.4$ meV/f.u. is the energy difference between ferromagnetic and zigzag antiferromagnetic states, and M is the Ni magnetic moment. We find a spin-flop field of $B_{SF} = 7.2$ T for $Na_3Ni_2SbO_6$, which underestimates the experimental value but remains qualitatively of the same order of magnitude. The estimation for a spin-flip (saturation) field gives about 20 T, in good agreement with experimentally found value $B_{sat} \sim 23$ T.

G. Magnetic phase diagrams

Summarizing the data, the magnetic phase diagrams for the new layered antimonates $A_3Ni_2SbO_6$ (A = Li, Na) can be suggested (Fig. 12). At temperatures above T_N in zero magnetic field, the paramagnetic phase is realized. With increasing the magnetic field, this phase transition boundary shifts slowly to the lower-temperature side. The antiferromagnetic state, however, is complicated by presence of two more field-induced phases at low temperatures. The quantum ground state determined as a zigzag antiferromagnetic state (AF1) exists below 5 T for $Li_3Ni_2SbO_6$ and 10 T for $Na_3Ni_2SbO_6$, respectively. The field-induced spin-flop phase (AF2) was found to be realized in the field ranges 5–15 T for $Li_3Ni_2SbO_6$ and 10–18 T for $Na_3Ni_2SbO_6$, and those are replaced by another field-induced antiferromagnetic phase (AF3), which most probably corresponds to another spin configuration. The spin-flip transition is realized at 20 and 23 T for $Li_3Ni_2SbO_6$ and $Na_3Ni_2SbO_6$, respectively. These observations are well accounted for by DFT calculations for the main magnetic exchange interactions, which show that both the antiferromagnetic and ferromagnetic intralayer spin exchanges are present on the honeycomb planes, resulting in a zigzag antiferromagnetic ground state on the honeycomb lattice. Neutron scattering studies in applied magnetic fields would be desirable for determination of actual spin configurations in the AF1, AF2, and AF3 phases.

IV. CONCLUSION

In conclusion, we have examined the thermodynamic and resonance properties of two layered honeycomb lattice monoclinic oxides $A_3Ni_2SbO_6$ (A = Li, Na) by both bulk (magnetic susceptibility, magnetization, and specific heat) and local (ESR and NMR) experimental techniques and by performing DFT calculations. The overall results are consistent with each other and yield the picture of a complex magnetic ordering at low temperatures. Magnetic susceptibility and specific heat data indicate the onset of antiferromagnetic long-range order. In addition, the magnetization curves reveal a field-induced (spin-flop type) transition below T_N that can be understood in terms of the magnetocrystalline anisotropy in these systems. ESR and NMR show the presence of appreciable low-dimensional (short-range) correlations below ~100 K. The theoretical calculations show that interplane exchange coupling is very weak for both compounds, so that they both can be considered 2D magnets. At the same time, both ferromagnetic and antiferromagnetic intraplane exchange interactions are present on the honeycomb Ni_2SbO_6 layers, and the most favorable spin configuration model is zigzag ferromagnetic chains coupled antiferromagnetically. This magnetic configuration is well compatible with our NMR data.

ACKNOWLEDGMENTS

The work was supported by the Russian Foundation for Basic Research (Grants No. 11-03-01101 to E.A.Z. and V.B.N., No. 14-02-00245 to E.A.Z., E.L.V., and M.I.S., and No. 14-02-01194 to E.L.V. and M.F.I.). The work of M.A. and A.V.S. was supported by the crédit de démarrage U.Lg. M.A. thanks Jun Li [Institute for Nanoscale Physics and Chemistry (INPAC), Katholieke Universiteit Leuven (K. U. Leuven)] for assistance in measurements and H.-L. Feng and K. Yamaura

(National Institute for Materials Science, Japan) for discussion of specific heat data. H.O.J. and R.V. thank the Deutsche Forschungsgemeinschaft (DFG) for financial support through SFB/TR49. A.N.V. acknowledges support from the Ministry of Education and Science of the Russian Federation in the framework Increase Competitiveness Program of NUST «MISiS» (Grant No. K2-2014-036). The authors thank L. I. Medvedeva and M. A. Evstigneeva for providing samples used for the present paper. A.S. and S.P. acknowledge support from CARIPLO Foundation through MAGISTER Project No. Rif. 2013-0726 and from Italian Ministry of Research through Project No. PRIN-2010 "Interfacce di ossidi: nuove proprieta' emergenti, multifunzionalita' e dispositivi per l'elettronica e l'energia (OXIDE)."

[1] B. Xu, D. Qian, Z. Wang, and Y. S. Meng, Mater. Sci. Eng. R **73**, 51 (2012).
[2] J. B. Goodenough, J. Solid State Electrochem. **16**, 2019 (2012).
[3] I. Terasaki, Y. Sasago, and K. Uchinokura, Phys. Rev. B **56**, R12685 (1997).
[4] M. Lee, L. Viciu, L. Li, Y. Wang, M. L. Foo, S. Watauchi, R. A. Pascal Jr., R. J. Cava, and N. P. Ong, Nat. Mater. **5**, 537 (2006).
[5] K. Takada, H. Sakurai, E. Takayama-Muromachi, F. Izumi, R. A. Dilanian, and T. Sasaki, Nature **422**, 53 (2003).
[6] J. D. Jorgensen, M. Avdeev, D. G. Hinks, J. C. Burley, and S. Short, Phys. Rev. B **68**, 214517 (2003).
[7] C. Greaves and S. M. A. Katib, Mater. Res. Bull. **25**, 1175 (1990).
[8] G. C. Mather, C. Dussarrat, J. Etourneau, and A. R. West, J. Mater. Chem. **10**, 2219 (2000).
[9] R. Nagarajan, S. Uma, M. K. Jayaraj, J. Tate, and A. W. Sleight, Solid State Sci. **4**, 787 (2002).
[10] J. Xu, A. Assoud, N. Soheilnia, S. Derakhshan, H. L. Cuthbert, J. E. Greedan, M. H. Whangbo, and H. Kleinke, Inorg. Chem. **44**, 5042 (2005).
[11] S. Derakhshan, H. L. Cuthbert, J. E. Greedan, B. Rahaman, and T. Saha-Dasgupta, Phys. Rev. B **76**, 104403 (2007).
[12] Y. Miura, R. Hirai, Y. Kobayashi, and M. Sato, J. Phys. Soc. Japn. **75**, 084707 (2006).
[13] Y. Miura, R. Hirai, T. Fujita, Y. Kobayashi, and M. Sato, J. Magn. Magn. Mater. **310**, e389 (2007).
[14] Y. Miura, Y. Yasui, T. Moyoshi, M. Sato, and K. Kakurai, J. Phys. Soc. Jpn. **77**, 104709 (2008).
[15] C. N. Kuo, T. S. Jian, and C. S. Lue, J. Alloys Comp. **531**, 1 (2012).
[16] O. A. Smirnova, V. B. Nalbandyan, A. A. Petrenko, and M. Avdeev, J. Solid State Chem. **178**, 1165 (2005).
[17] W. Schmidt, R. Berthelot, A. W. Sleight, and M. A. Subramanian, J. Solid State Chem. **201**, 178 (2013).
[18] R. Berthelot, W. Schmidt, A. W. Sleight, and M. A. Subramanian, J. Solid State Chem. **196**, 225 (2012).
[19] L. Viciu, Q. Huang, E. Morosan, H. W. Zandbergen, N. I. Greenbaum, T. McQueen, and R. J. Cava, J. Solid State Chem. **180**, 1060 (2007).
[20] E. A. Zvereva, M. A. Evstigneeva, V. B. Nalbandyan, O. A. Savelieva, S. A. Ibragimov, O. S. Volkova, L. I. Medvedeva, A. N. Vasiliev, R. Klingeler, and B. Buechner, Dalton Trans. **41**, 572 (2012).
[21] R. Berthelot, W. Schmidt, S. Muir, J. Eilertsen, L. Etienne, A. W. Sleight, and M. A. Subramanian, Inorg. Chem. **51**, 5377 (2012).
[22] V. V. Politaev, V. B. Nalbandyan, A. A. Petrenko, I. L. Shukaev, V. A. Volotchaev, and B. S. Medvedev, J. Solid State Chem. **183**, 684 (2010).
[23] M. A. Evstigneeva, V. B. Nalbandyan, A. A. Petrenko, B. S. Medvedev, and A. A. Kataev, Chem. Mater. **23**, 1174 (2011).
[24] V. Kumar, N. Bhardwaj, N. Tomar, V. Thakral, and S. Uma, Inorg. Chem. **51**, 10471 (2012).
[25] V. Kumar, A. Gupta, and S. Uma, Dalton Trans. **42**, 14992 (2013).
[26] V. B. Nalbandyan, M. Avdeev, and M. A. Evstigneeva, J. Solid State Chem. **199**, 62 (2013).
[27] V. B. Nalbandyan, A. A. Petrenko, and M. A. Evstigneeva, Solid State Ionics **233**, 7 (2013).
[28] E. A. Zvereva, O. A. Savelieva, Ya. D. Titov, M. A. Evstigneeva, V. B. Nalbandyan, C. N. Kao, J.-Y. Lin, I. A. Presniakov, A. V. Sobolev, S. A. Ibragimov, M. Abdel-Hafiez, Yu. Krupskaya, C. Jähne, G. Tan, R. Klingeler, B. Büchner, and A. N. Vasiliev, Dalton Trans. **42**, 1550 (2013).
[29] J. H. Roudebush and R. J. Cava, J. Solid State Chem. **204**, 178 (2013).
[30] E. Climent-Pascual, P. Norby, N. H. Andersen, P. W. Stephens, H. W. Zandbergen, J. Larsen, and R. J. Cava, Inorg. Chem. **51**, 557 (2012).
[31] J. H. Roudebush, N. H. Andersen, R. Ramlau, V. O. Garlea, R. Toft-Petersen, P. Norby, R. Schneider, J. N. Hay, and R. J. Cava, Inorg. Chem. **52**, 6083 (2013).
[32] A. Gupta, C. B. Mullins, and J. B. Goodenough, J. Power Sources **243**, 817 (2013).
[33] E. M. Seibel, J. H. Roudebush, H. Wu, Q. Huang, M. N. Ali, H. Ji, and R. J. Cava, Inorg. Chem. **52**, 13605 (2013).
[34] W. Schmidt, R. Berthelot, L. Etienne, A. Wattiaux, and M. A. Subramanian, Mater. Res. Bull. **50**, 292 (2014).
[35] M. Schmitt, O. Janson, S. Golbs, M. Schmidt, W. Schnelle, J. Richter, and H. Rosner, Phys. Rev. B **89**, 174403 (2014).
[36] N. Bhardwaj, A. Gupta, and S. Uma, Dalton Trans. **43**, 12050 (2014).
[37] A. Mulder, R. Ganesh, L. Capriotti, and A. Paramekanti, Phys. Rev. B **81**, 214419 (2010).
[38] P. H. Y. Li, R. F. Bishop, D. J. J. Farnell, and C. E. Campbell, Phys. Rev. B **86**, 144404 (2012).
[39] J. Ma, S.-H. Bo, L. Wu, Y. Zhu, C. P. Grey, and P. G. Khalifah, Chem. Mater. **27**, 2387 (2015).
[40] K. Koepernik and H. Eschrig, Phys. Rev. B **59**, 1743 (1999).
[41] J. P. Perdew, K. Burke, and M. Ernzerhof, Phys. Rev. Lett. **77**, 3865 (1996).
[42] G. Kresse and J. Furthmüller, Phys. Rev. B **54**, 11169 (1996).
[43] K. Foyevtsova, I. Opahle, Y.-Z. Zhang, H. O. Jeschke, and R. Valentí, Phys. Rev. B **83**, 125126 (2011).
[44] U. Tutsch, B. Wolf, S. Wessel, L. Postulka, Y. Tsui, H. O. Jeschke, I. Opahle, T. Saha-Dasgupta, R. Valentí, A. Brühl, K. Remović-Langer, T. Kretz, H.-W. Lerner, M. Wagner, and M. Lang, Nature Comm. **5**, 5169 (2014).

[45] J. P. Joshi and S. V. Bhat, J. Magn. Res. **168**, 284 (2004).
[46] H.-A. Krug von Nidda, L. E. Svistov, M. V. Eremin, R. M. Eremina, A. Loidl, V. Kataev, A. Validov, A. Prokofiev, and W. Aßmus, Phys. Rev. B **65**, 134445 (2002).
[47] J. M. Law, P. Reuvekamp, R. Glaum, C. Lee, J. Kang, M.-H. Whangbo, and R. K. Kremer, Phys. Rev. B **84**, 014426 (2011).
[48] V. B. Nalbandyan, E. A. Zvereva, G. E. Yalovega, I. L. Shukaev, A. P. Ryzhakova, A. A. Guda, A. Stroppa, S. Picozzi, A. N. Vasiliev, and M.-H. Whangbo, Inorg. Chem. **52**, 11850 (2013).
[49] E. A. Zvereva, V. B. Nalbandyan, M. A. Evstigneeva, H.-J. Koo, M.-H. Whangbo, A. V. Ushakov, B. S. Medvedev, L. I. Medvedeva, N. A. Gridina, G. E. Yalovega, A. V. Churikov, A. N. Vasiliev, and B. Büchner, J. Solid State Chem. **225**, 89 (2015).
[50] L. J. de Jongh and A. R. Miedema, Adv. Phys. **23**, 1 (1974).
[51] J. E. Greedan, J. Mater. Chem. **11**, 37 (2001).
[52] K. Kawasaki, Prog. Theor. Phys. **39**, 285 (1968).
[53] K. Kawasaki, Phys. Lett. A **26**, 543 (1968).
[54] H. Mori and K. Kawasaki, Prog. Theor. Phys. **28**, 971 (1962).
[55] D. L. Huber, Phys. Rev. B **6**, 3180 (1972).
[56] P. M. Richards and M. B. Salamon, Phys. Rev. B **9**, 32 (1974).
[57] R. D. Willett and F. Waldner, J. Appl. Phys. **53**, 2680 (1982).
[58] R. D. Willett and R. Wong, J. Magn. Res. **42**, 446 (1981).
[59] T. G. Castner Jr. and M. S. Seehra, Phys. Rev. B **4**, 38 (1971).
[60] T. G. Castner and M. S. Seehra, Phys. Rev. B **47**, 578 (1993).
[61] M. Heinrich, H.-A. Krug von Nidda, A. Loidl, N. Rogado, and R. J. Cava, Phys. Rev. Lett. **91**, 137601 (2003).
[62] A. Zorko, F. Bert, A. Ozarowski, J. van Tol, D. Boldrin, A. S. Wills, and P. Mendels, Phys. Rev. B **88**, 144419 (2013).
[63] D. L. Huber and M. S. Seehra, J. Phys. Chem. Solids **36**, 723 (1975).
[64] M. S. Seehra, M. M. Ibrahim, V. S. Babu, and G. Srinivasan, J. Phys.: Condens. Matter **8**, 11283 (1996).
[65] A. Zorko, D. Arčon, H. van Tol, L. C. Brunel, and H. Kageyama, Phys. Rev. B **69**, 174420 (2004).
[66] J. H. Roudebush, G. Sahasrabudhe, S. L. Bergman, and R. J. Cava, Inorg. Chem. **54**, 3203 (2015).
[67] M. E. Fisher, Proc. Roy. Soc. (London) A **254**, 66 (1960).
[68] M. E. Fisher, Phil. Mag. **7**, 1731 (1962).
[69] R. L. Carlin, *Magnetochemistry* (Springer-Verlag, Berlin, 1986).
[70] A. Tari, *The Specific Heat of Matter at Low Temperature*, (Imperial College Press, London, 2003).
[71] H. Benner and J. P. Boucher, *Spin Dynamics in the Paramagnetic Regime: NMR and EPR in Two-Dimensional Magnets—"Magnetic Properties of Layered Transition Metal Compounds"*, edited by L. J. de Jongh (Springer, Netherlands, 1990), p. 323.
[72] M. Yehia, E. Vavilova, A. Möller, T. Taetz, U. Löw, R. Klingeler, V. Kataev, and B. Büchner, Phys. Rev. B **81**, 060414 (2010).
[73] C. P. Slichter, *Principles of Magnetic Resonance*, Springer Series in Solid-State Sciences 1, Third Edition (Springer-Verlag, Berlin, Heidelberg, New York, 1990).
[74] Y. Yamada and A. Sakata, J. Phys. Soc. Jpn. **55**, 1751 (1986).
[75] Y. Fujii, H. Kikuchi, T. Arai, Y. Tanabe, K. Kindo, and A. Matsuo, J. Phys.: Conf. Series **200**, 022009 (2010).
[76] Y. Ideta, Y. Kawasaki, Y. Kishimoto, T. Ohno, Y. Michihiro, Z. He, Y. Ueda, and M. Itoh, Phys. Rev. B **86**, 094433 (2012).
[77] Note, however, that the given value actually corresponds to a sum of interlayer couplings $J_5 + J_6$, as more effort would be required to distinguish the interlayer couplings. Considering the size compared to J_1 and J_2 however, this is not necessary.
[78] A. Lohmann, H.-J. Schmidt, and J. Richter, Phys. Rev. B **89**, 014415 (2014).
[79] M. D. Watson, A. McCollam, S. F. Blake, D. Vignolles, L. Drigo, I. I. Mazin, D. Guterding, H. O. Jeschke, R. Valentí, N. Ni, R. Cava, and A. I. Coldea, Phys. Rev. B **89**, 205136 (2014).